nature communications

Article

https://doi.org/10.1038/s41467-024-51952-z

Alphavirus nsP3 organizes into tubular scaffolds essential for infection and the cytoplasmic granule architecture

Received: 30 June 2024

Accepted: 20 August 2024

Published online: 16 September 2024

Check for updates

Vasiliya Kril[1,10], Michael Hons[2,9,10], Celine Amadori[1], Claire Zimberger[3], Laurine Couture[1], Yara Bouery[1], Julien Burlaud-Gaillard[4], Andrei Karpov[5,6], Denis Ptchelkine[3], Alexandra L. Thienel[7], Beate M. Kümmerer[7], Ambroise Desfosses[8], Rhian Jones[3,6], Philippe Roingeard[4], Laurent Meertens[1], Ali Amara[1,11] ✉ & Juan Reguera[3,6,11] ✉

Alphaviruses, such as chikungunya virus (CHIKV), are mosquito-borne viruses that represent a significant threat to human health due to the current context of global warming. Efficient alphavirus infection relies on the activity of the non-structural protein 3 (nsP3), a puzzling multifunctional molecule whose role in infection remains largely unknown. NsP3 is a component of the plasma membrane-bound viral RNA replication complex (vRC) essential for RNA amplification and is also found in large cytoplasmic aggregates of unknown function. Here, we report the cryo-electron microscopy (cryo-EM) structure of the CHIKV nsP3 at 2.35 Å resolution. We show that nsP3 assembles into tubular structures made by a helical arrangement of its alphavirus unique domain (AUD). The nsP3 helical scaffolds are consistent with crown structures found on tomographic reconstructions of the mature viral RCs. In addition, nsP3 helices assemble into cytoplasmic granules organized in a network of tubular structures that contain viral genomic RNA and capsid as well as host factors required for productive infection. Structure-guided mutagenesis identified residues that prevent or disturb nsP3 assemblies, resulting in impaired viral replication or transcription. Altogether, our results reveal an unexpected nsP3-dependent molecular organization essential for different phases of alphavirus infection.

Alphaviruses are mosquito-borne viruses causing neurological and arthritogenic diseases in humans than can persist months to years after the initial infection[1]. They are enveloped RNA viruses with a single-strand positive RNA organized in two open reading frames (ORFs)[2,3]. The 5′ ORF encodes the P1234 polyprotein that is processed to generate four non-structural proteins (nsP1 to 4) which assemble into vRCs and are also involved in immune evasion (Fig. 1a)[2,3]. The 3′ ORF is transcribed into a sub-genomic (sg) positive-strand RNA and encodes the structural proteins important for virus assembly and budding (Fig. 1a)[2,3]. Alphavirus replication starts with the synthesis of a double-

[1]Université de Paris-Cité, Biology of Emerging Viruses Team, INSERM U944/CNRS UMR 7212, Institut de Recherche Saint-Louis, Hôpital Saint Louis, Paris, France. [2]European Molecular Biology Laboratory, Grenoble, France. [3]Aix-Marseille Université, CNRS, AFMB UMR 7257 Marseille, France. [4]Université de Tours, INSERM U1259 MAVIVH et Plateforme IBiSA de Microscopie Electronique, Tours, France. [5]Aix-Marseille Université, CNRS, AFMB UMR 7257, Turing Centre for Living Systems, 13288 Marseille, France. [6]Viral Macromolecular Complexes Team, ERL-INSERM U1324 Marseille, France. [7]Institute of Virology, Medical Faculty, University of Bonn, Bonn, Germany. [8]Institut de Biologie Structurale, Université Grenoble Alpes, CEA, CNRS, IBS, Grenoble, France. [9]Present address: CSSB Centre for Structural Systems Biology, Deutsches Elektronen Synchrotron DESY, Hamburg, Germany. [10]These authors contributed equally: Vasiliya Kril, Michael Hons. [11]These authors jointly supervised this work: Ali Amara, Juan Reguera. ✉e-mail: ali.amara@inserm.fr; juan.reguera@inserm.fr

https://doi.org/10.1038/s41467-024-51952-z

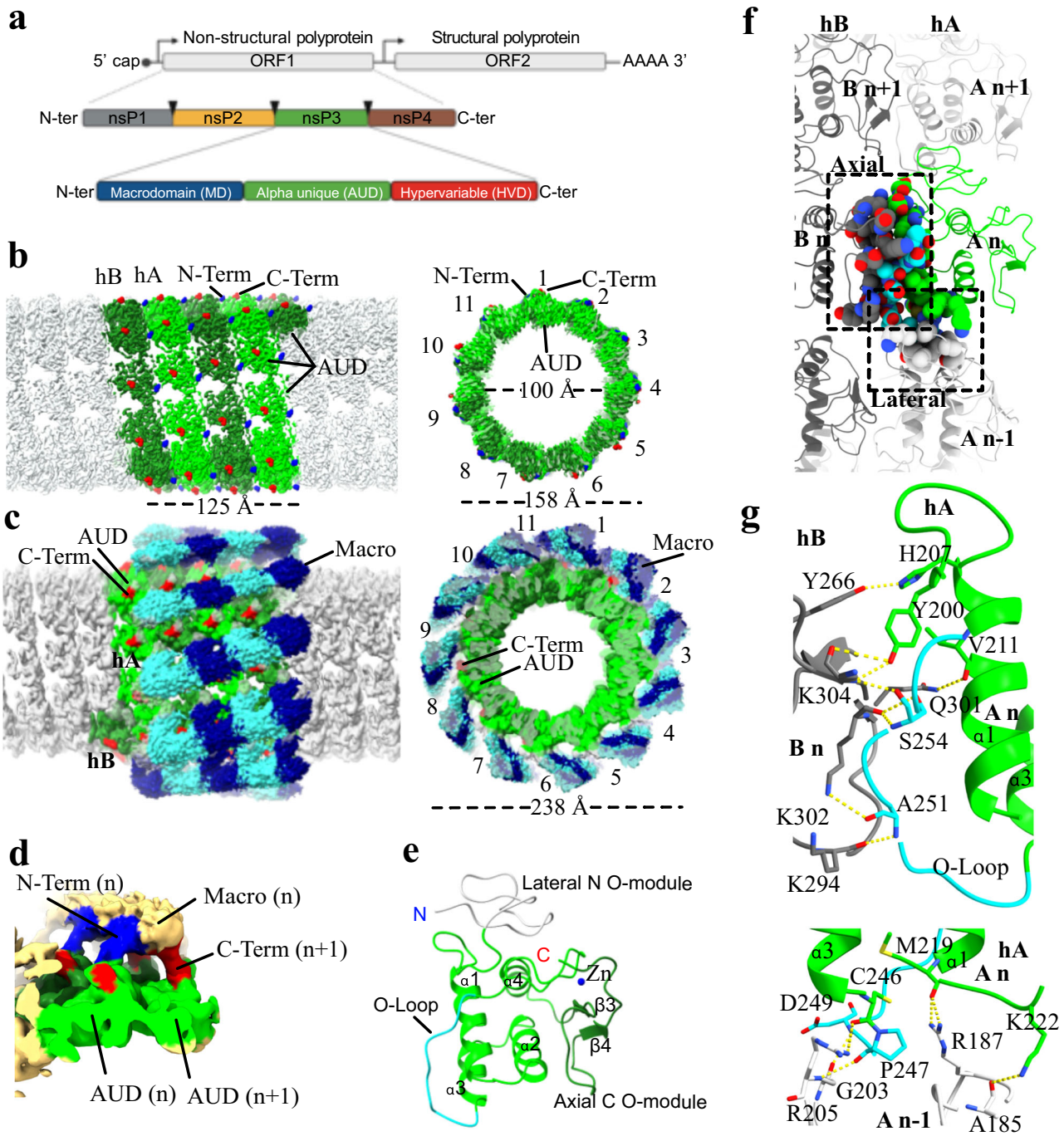

strand viral RNA (dsRNA) intermediate[3,4]. This process is coupled to the formation of invaginations of the plasma membrane called spherules that house the vRC, dsRNA and cellular factors[2,3]. RNA synthesis is regulated by the sequential cleavage of the P1234 polyprotein by the nsP2-associated protease[3,5]. A first cleavage generates the P123 precursor and nsP4 which form the early vRC synthetizing negative strand RNA intermediate[6]. P123 precursor is further processed into mature nsPs that organize the late replicase complex which synthetizes new positive sense genomic RNA and sgRNAs but can no longer produce negative strand genomes[3]. The molecular mechanisms that lead to the maturation of the vRC are still poorly understood and appear to involve conformational changes rather than depending exclusively on polyprotein processing[7].

Recent structural and functional characterization of the CHIKV mature vRC in vitro and in infected cells provided insights into the architecture of fully proteolytically processed vRC[8,9]. The viral polymerase nsP4, which forms a complex with nsP2 helicase-protease, sits in the central pore of the membrane-anchored dodecameric nsP1 RNA-capping ring[8–10]. The nsP3 protein is elusive in these structural studies and is thought to be part of a cytoplasmic crown found above nsP1 capping rings. Very few structural information are available for nsP3. It comes mainly from a crystal structure of a uncleaved form nsP23 construct from Sindbis virus (SINV) comprising the methyltransferase-like (MTase) and protease (Pro) domains of nsP2 forming a U-shaped structure with the Alphavirus Unique Domain (AUD) and the Macrodomain (MD) of nsP3, mostly through interactions between Pro and

Fig. 1 | Structure of CHIKV nsP3 helical scaffolds (HSs). a Alphavirus genomic organization and nsP3 domains. **b** Cryo-EM map of nsP3 HSs at 2.52 Å resolution (EMD: 17729) is represented in light gray. The left panel shows a longitudinal view of the scaffold with two turns of the two-start helix of AUD domains (hA and hB) colored in light and dark green, respectively. The N and C terminus of each protomer are colored in blue and red, respectively. The right panel shows a transversal section of the same structure, 11 protomers per turn are visible, the dimensions of the internal and external diameter of the AUD scaffold are indicated. **c** same representation of the cryo-EM map calculated with a larger mask at 2.98 Å resolution (EMBD: 17730) colored in dark gray. Additional densities corresponding to the MD are visible and colored in cyan and blue for the hA and hB, respectively. The right panel shows the transversal section of the structure as in (**a**). The outer diameter of the scaffold including the MDs is indicated. **d** Cryo-EM map after local 3D classification at 6.4 Å resolution (EMBD: 17730) is shown in yellow. The AUDs are colored in light green and labeled. The N and C terminus of the AUD are colored in blue and red respectively. This map shows the connection of the AUD N terminus with the density corresponding to the MD, and also the interaction of the beginning of the HVD at the C terminus of the nearby AUD $n+1$ contacting the protomer n MD. **e** Cartoon representation of the AUD domain with the oligomerization modules (O-modules) which mediate lateral and axial contacts colored in light gray and dark green, respectively, and labeled. The oligomerization loop, which mediates contacts in both axial and lateral interface, is colored in cyan and labeled. **f** The interprotomer interactions are shown in the context of the helical scaffold. The two helices of AUD, hA and hB, are represented in light and dark cartoons and labeled. The AUD An is colored in green and the residues mediating interprotomer contacts are shown in spheres and colored as in panel d. The residues mediating contacts from Bn and A $n-1$ protomers are also shown in spheres. The axial (Bn/An) and lateral (An/An-1) interfaces are indicated by dashed line squares. **g** Detailed representation of axial and lateral contacts between AUDs are shown in the upper and bottom panels, respectively. AUDs are labeled, represented in cartoon and colored as in panel (**e**). The residues mediating interprotomer contacts are shown in sticks and labeled. Hydrogen bonds are shown by yellow dashed lines.

AUD domains[11]. Besides, the complete architecture of the RCs before or after the conformational transition and proteolytic cleavage governing RNA synthesis remains obscure.

NsP3 is composed of three domains, the MD which recognizes and hydrolyzes ADP ribosylated proteins[12], a conserved AUD required for RNA synthesis[13], and a hypervariable domain (HVD) mediating extensive host interactions important for viral replication and adaptation to the host (Fig. 1a)[14,15]. NsP3 is essential for viral replication[11,13], however, in contrast to the other nsPs, its precise function remains poorly understood. Our knowledge is mostly limited to the ability of nsP3 HVD to recruit host factors important for viral infection and the studies showing that mutations in the MD or AUD making viruses non-viable[11,13–15]. During the early phase of infection, nsP3 localizes at the cytoplasmic side of the viral spherules and is important for vRNA synthesis[3]. As the infection progresses, nsP3 assembles into enigmatic cytoplasmic granules (also called nsP3 puncta, foci, aggregates or condensates and referred here as "alpha-granules") that are a hallmark of alphavirus infection[2,16]. Alpha-granules are believed to sequester the Ras GTPase-activating protein-binding proteins (G3BPs), resulting on inhibition of stress granules formation[16].

Here, we present the cryo-EM structure of CHIKV nsP3 at 2,35 Å resolution. We show that nsP3 polymerizes via its AUD domain to generate helical scaffolds (HSs) important for infection. NsP3 HSs are consistent with the crown found in alphavirus fully-processed vRCs and define the internal architecture of alpha-granules.

Results

Atomic structure of alphavirus nsP3 helical scaffolds (HSs)

We expressed the CHIKV nsP3 in Hi-5 insect cells and purify it by consecutive affinity and size exclusion chromatography at 0.5 M NaCl. This yielded both monomeric and high-molecular-weight nsP3 species (Supplementary Fig. 1a). Analysis by negative staining electron microscopy (NS-EM) revealed that the latter correspond to tubular macro-complexes harboring a well-defined internal cavity delimited by a weakly structured matrix and surrounded by a jelly-like shield (Supplementary Fig. 1b). The CHIKV nsP3 monomers can re-assemble in vitro by lowering salt concentration (Supplementary Fig. 1c). Similar experimental procedures were applied to nsP3 of SINV and Eastern Equine Encephalitis virus (EEEV) but the HSs did not disassemble at high salt concentrations. In consequence we could only detect HSs by NS-EM in either small fragments after size exclusion chromatography or large aggregates after affinity chromatography for SINV and EEEV, respectively (Supplementary Fig. 1b). We then determined the structure of the CHIKV nsP3 tubes by cryo-electron microscopy (cryo-EM) at 2.52 Å resolution (EMD: 17729, Supplementary Fig. 2, Supplementary Fig. 3 and Table 1). Local refinement allowed to reach 2.36 Å on which we refined the AUD structure from an Alphafold2 prediction (EMD: 17678; PDB: 8PHZ, Supplementary Fig. 4, Table 1) and reconstituted the helical assembly (PDB: 8PK7). We found that the tubes are made by a helical arrangement of the nsP3 AUD with an axial rise of 2.782 Å and a helical twist of -164.175 ° (Supplementary Fig. 5, see methods section). Lateral views clearly reveal the existence of two-start parallel helixes (hA and hB) with a right-handed arrangement of the AUD (Fig. 1b). Each helix has 11.37 protomers per turn (Fig. 1b). The assembly generates interstitial positively charged pores connecting the inner cavity with the exterior, which could accommodate small negatively charged molecules like RNA (Fig. 2a, b). Although barely visible in the structure due to their high flexibility, the N-terminal MD and the C-terminal HVD, are clearly projected to the outside of the tubular structure (Fig. 1c). Refinement using a larger mask yielded a lower resolution map of the helical particles (2.98 Å resolution, EMD: 17730) with discernable globular appendices that can be assigned to the MD by main-chain connectivity (Fig. 1d). The MD of each nsP3 protomer is lying on the next AUD (hA n+1) of the same helix. A 3D focused classification provided one 3D class clearly showing the beginning of the HVD interacting with the MD of the hA n-1 protomer (Fig. 1d, Supplementary Fig. 2, EMD: 17730). Because of the low resolution of the map (6.84 Å), we could not deduce the exact position of contacts between the MD and HVDs, which are connected to the AUD through long flexible linkers. Beside these limitations, the structure clearly shows that MD-MD and HVD-MD interactions build a flexible and structured shield on the exterior of the tube which contributes to the interprotomer interactions. The projection of the HVD on the outside of the tube (Fig. 1c, d) is of particular interest considering its function as an assembly hub for the recruitment of host factors[14,15]. HVD–MD proximity may favor the specific de-ribosylation of HVD interactors such as G3BPs. The flexibility of the perimetral region of the tube including the MD and HVD would increase the maneuver range of the MD active site to reach different ADP-ribosylated regions of the HVD-binding host proteins[12].

The nsP3 AUD is an oligomerization module which is blocked in the nsP2-3 polyprotein

The structure of CHIKV HSs reveals the oligomerization elements harbored in the AUD folding (Fig. 1e and sequence alignment in Supplementary Fig. 6). The nsP3 AUD consists of four alpha helixes (α1-α4) with extensions at the N and C terminus acting as oligomerization modules (N and C O-modules) responsible for lateral and axial contacts with the AUD of neighboring protomers, respectively. The lateral and axial interfaces bury 320 Å^2 and 530 Å^2 of surface area, respectively (Fig. 1f). The O-modules are rich in positively charged residues and hold the core of neighboring protomers interacting with two regions including residues Y200 to K222 and R243 to P257 (Fig. 1g). The R243 to P257 region contains an acidic amino acid-rich loop flanked by C246 and P257 residues (O-loop) which adopts a slightly different conformation as compared to the CHIKV-predicted Alphafold2 structure[17], consistent with previous structures reported for SINV[11]

Table 1 | Cryo-EM data collection, processing, and model refinement statistics

Sample	PDB: 8PK7 EMD-17729	PDB: 8PHZ EMD-17678	EMD-17730	EMD-17730 Supplementary map
Grids	QF 2/1 300 mesh (Cu)	QF 2/1 300 mesh (Cu)	QF 2/1 300 mesh (Cu)	QF 2/1 300 mesh (Cu)
Vitrification method	Vitrobot	Vitrobot	Vitrobot	Vitrobot
Microscope	Titan Krios G3, CM01, ESRF	Titan Krios G3, CM01, ESRF	Titan Krios G3, CM01, ESRF	Titan Krios G3, CM01, ESRF
Magnification factor	81,000	81,000	81,000	81,000
Detector	K3 Summit (Gatan)	K3 Summit (Gatan)	K3 Summit (Gatan)	K3 Summit (Gatan)
Recording mode	Super-resolution	Super-resolution	Super-resolution	Super-resolution
Electron dose rate ($e^{-}Å^{-2}s^{-1}$)	18.1	18.1	18.1	18.1
Total electron dose ($e^{-}Å^{-2}$)	42	42	42	42
Pixel size (Å)	1.06 (nominal) 0.53 (super-resolution)	1.06 (nominal) 0.53 (super-resolution)	1.06 (nominal) 0.53 (super-resolution)	1.06 (nominal) 0.53 (super-resolution)
Number of frames	40	40	40	40
Total exposure time (s)	2.6	2.6	2.6	2.6
Set defocus range (μm)	0.8–2.5	0.8-2.5	0.8-2.5	0.8-2.5
Number of micrographs	13,046	13,046	13,046	13,046
Number of picked particles	807,973	807,973	807,973	807,973
Number of particles used for refinement	807,973	9,695,676 (12x symmetry expanded)	807,973	250,100
Symmetry imposed	Helical, C1, twist: 164.175°, rise (Å): 2.782, symmetry order: 12	C1	Helical, C1, twist: 164.175°, rise (Å): 2.782, symmetry order: 12	C1
Resolution (Å) (half-map half-map, FSC threshold 0.143)	2,52	2,36	2,98	6,84
RMSD bonds (Å)	0,004	0,003		
RMDS angles (°)	0,932	0,523		
Ramachandran favored (%)	99,4	99,4		
Ramachandran outliers (%)	0,00	0,00		
Rotamer outliers (%)	0,00	0,00		
Map-model cross correlation (CC, main chain)	0,73	0,81		
Clashscore	9,26	8,38		
MolProbity score	1,49	1,45		
Map-model FSC (Å) (threshold = 0.5)	3,0	2,5		

(Supplementary Fig. 6c). The O-loop mediates extensive interactions with both N- and C O-modules from hA n-1 and hB n-protomers, respectively. Even if no stable salt bridges are observed in the structure, the charge distribution is suggestive of an interaction of electrostatic nature (Fig. 2b, c) consistent with our experiments showing that high salt concentrations promote filament disassembly in vitro (Supplementary Fig. 1c). In addition, a network of hydrogen bonds woven by residues A251, S254, V211, Y200 with residues H207, Y266, K304, Q301 and K302 of hB n-protomer seals the axial contacts. Likewise, residues M219, K222, D249 and C246 coordinate h-bonds with R187, A185, G203 and R205, stabilizing the lateral interface (Fig. 1g).

The superposition of HSs AUD on the structure of the uncleaved SINV nsP2-nsP3 polyprotein[11] shows that the residues in the O-loop which mediate axial contacts are totally buried by the nsP2 protease domain, comprising other important residues for oligomerization like Y200 which is at the center of the interface (Fig. 3a, b). Conversely, the residues mediating axial contacts in the C O-module and the residues mediating lateral contacts in the O-Loop and N O-module are still exposed to the solvent. This conformational state would prevent HSs assembly in the axial direction but allows oligomerization in the lateral direction.

NsP3 assemblies are part of the viral replication complex

NsP3 is a component of the vRC. Tomographic reconstruction of CHIKV spherule necks revealed the vRC architecture with a molecular pore delineated by a nsP1 dodecamer ring connected to a larger tubular structure (crown) in its cytoplasmic side[8,9]. Superposition of nsP3 HSs into the crowns shows similar dimensions and shape (Fig. 4). The tomographic reconstruction of the vRC reported by Laurent et al[8]. shows perimetral volumes which correlate well in the superposition with the nsP3 MDs (Fig. 4a). This is lost in higher resolution volumes reported by Tan et al.[9] (Fig. 4b). For both tomographic reconstructions a 12-fold symmetry (C12) was imposed to the calculated volumes which is consistent with nsP1 capping pores[10]. The reported unsymmetrized volumes do not allow to discern between helical or radial symmetry of the nsP3 crown due to the limited number of averaged tomograms. Our high-resolution data suggest that nsP3 could have a helical symmetry but a slight shift on the helix rise could result on the formation of superposed rings. In both cases, we would observe a tubular scaffold with similar interprotomer interactions and arrangement of MD and HVD in the assembly. Importantly, both assemblies would require the release of the O-loop and the total proteolytic processing of the nsP polyprotein for oligomerization.

https://doi.org/10.1038/s41467-024-51952-z

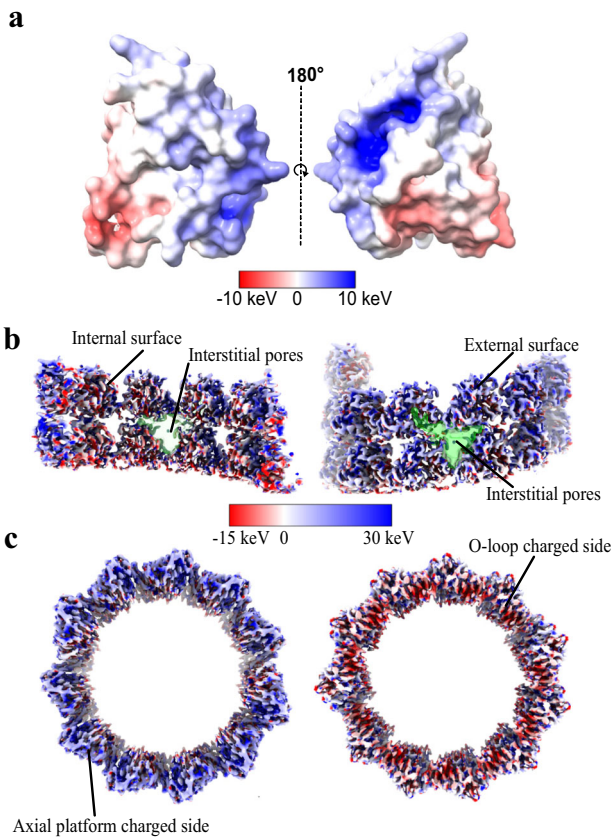

Fig. 2 | Analysis of charge distribution on the AUD helical scaffolds. a Surface charges representation of two sides of the AUD monomer. The monomer on the left has the same orientation than the monomer in Fig. 1e. The O-loop displays negative surface charges while the axial O-module, partly including the Zn finger, displays positive charges. **b** A section through the diameter of the scaffold shows the charge distribution of the interior which is rather neutral, equally combining positive and negative charges. The right panel shows the surface of the positively charged surface of the tubes. The positively charged interstitial pores of the helices connect with the external positive charged surface suggesting that naked RNA could transit the pores and bind the scaffold surface. **c** Same representation of the bottom and top of the HSs with positively and negatively charges, respectively, showing the electrostatic nature of the AUD oligomerization and helix formation. The surface electrostatics were calculated using APBS (https://www.poissonboltzmann.org/) on the ranges indicated by the scale-bars for panel (**a**) and (**b**, **c**) respectively.

Helical arrangements of nsP3 AUD form tubular structures that define the architecture of alpha-granules

During the early step of CHIKV infection, nsP3 is located at the plasma membrane and co-localizes with the RCs (Supplementary Fig. 7a, visualized here using an anti-dsRNA mAb). As the infection progresses, nsP3 loses membrane localization and forms internal punctate dots that accumulate in large cytoplasmic granules over the time. These structures do not co-localize with the dsRNA and are thus distinct from vRCs[16,18] (Supplementary Fig. 7a, b). During the early phases of infection, the CHIKV alpha-granules appear globular and spherical (Supplementary Fig. 7a–d) while assembling into irregular internal structures up to 0.8 μm long at later stages. (Supplementary Fig. 7b–d). Of note, alpha-granule length and morphology varies depending on the CHIKV strain or lineage (Supplementary Fig. 7c–d). An average of 40 alpha-granules are formed per cell 24 h after infection. Expression of nsP3 from different alphavirus (CHIKV, ONNV, MAYV, EEEV) is sufficient to induce alpha-granule formation, independently of the presence of other viral components (Supplementary Fig. 7e, f). Consistent with our structural findings, alpha-granule formation depends on nsP2-nsP3 processing. Expression of the CHIKV P1234 precursor harboring mutations affecting the nsP2-nsP3 cleavage[5,19] strongly inhibits the assembly of alpha-granules (Fig. 5a–c).

Transmission electron microscopy studies performed on primary fibroblasts either infected by CHIKV-21 or expressing CHIKV nsP3 revealed that the alpha-granules are made by a higher order arrangement of tubular structures consistent in size and shape with nsP3 HSs (Fig. 6a–c, Supplementary Fig. 8a). Immunogold labeling of nsP3 confirmed the identity of these scaffolds (Supplementary Fig. 8a–d). Considering the density of nsP3 scaffolds in the granules (400 helix turns /μm^2) and the number of nsP3 protomers per μm in the HSs (3870 nsP3/μm), we estimate that 1.55 million nsP3 protomers would be present in 1 μm^3 of alpha-granules for CHIKV. The organization of the nsP3 tubular structures differs depending on the alphavirus type. For instance, CHIKV and ONNV show a honeycomb arrangement of tubes while those for EEEV and MAYV seem to be randomly oriented forming a less compact and intricate mesh (Fig. 6b). Confocal and electron microscopy studies show that the CHIKV-nsP3 tubes contain G3BPs and FHL1, a recently identified host factor that binds selectively CHIKV and ONNV nsP3 HVD[14,20] (Supplementary Fig. 8c). This strongly indicates that nsP3 tubular structures are formidable molecular traps sequestering host factors important for infection. Since the nsP3 tubular structures do not show any arrangement in vitro (Supplementary Fig. 1b), and that nsP3 HVDs of different alphaviruses interact with distinct virus-specific sets of cellular proteins[14,15,21], one can speculate that nsP3-binding host factors could contribute to shape the nsP3 high-ordered aggregates. Consistent with this, swapping the VEEV and SINV nsP3 HVD has been shown to mediate formation of distinct, virus-specific nsP3 complexes[22]. In infected cells, most of the nsP3 alpha-granules colocalize with both the viral capsid (Fig. 6d, Supplementary Fig. 8d) and the viral genomic RNA (Fig. 6d), but contain neither E2 nor nsP1 proteins (Supplementary Fig. 8d), suggesting that they are directly or indirectly regulating the preassembly of the viral nucleocapsids. This is in line with a study imaging the alphavirus capsid protein during virus replication in living cells[23].

NsP3 helical structures are essential for alpha-granule formation

The nsP3 AUD has an intrinsic oligomerization capacity and forms filaments when expressed in human cells[16] (Supplementary Fig. 9a, b). Indeed, nsP3 molecules lacking the AUD domain do not form alpha-granules and are diffusively distributed in the cytoplasm when compared to WT or MD- or HVD-deleted nsP3 variants (Supplementary Fig. 9a). To further characterized the role of this structure during viral infection, we first generated a panel of structure-based mutations aiming to disturb CHIKV nsP3 oligomerization in the context of the AUD alone (Supplementary Fig. 9b) or the full nsP3 (Supplementary Fig. 9c). We expressed the nsP3 variants by transfection in U2OS cells and investigated by immunofluorescence and confocal microscopy their ability to form filaments and alpha-granules (Supplementary Fig. 9c, d). The nsP3 mutants were similarly expressed but presented different phenotypes (Supplementary Fig. 9e). Mutants R187A/R205A, A252P, P255A, R187A, S254A/S255A, H207A, Q301A, A250W, D249G/A250G/D251G showed AUD filaments and nsP3 alpha-granule formation like their WT counterpart (Supplementary Fig. 9c, d). The AUD or nsP3 proteins harboring K302A/V303A, P247A/V248A or Y200A mutants showed a strong reduction of alpha-granule formation and presented a homogeneous distribution in the cell cytoplasm. (Fig. 7a, b, Supplementary Fig. 9c, d). Of note we detected no alpha-granule formation with the Y200A mutant. Similar data were obtained when the Y201A and P248A/V249A mutations were introduced in a WT SINV nsP3 plasmid (Supplementary Fig. 9e). We next purified the recombinant K302A/V303A, P247A/V248A and Y200A CHIKV nsP3 mutants as monomers and tested their capacity to oligomerize by negative staining electron microscopy. At the same protein concentration (0.2 mg/ml), K302A/V303A and P247A/V248A nsP3 molecules showed altered oligomerization properties with the formation of

https://doi.org/10.1038/s41467-024-51952-z

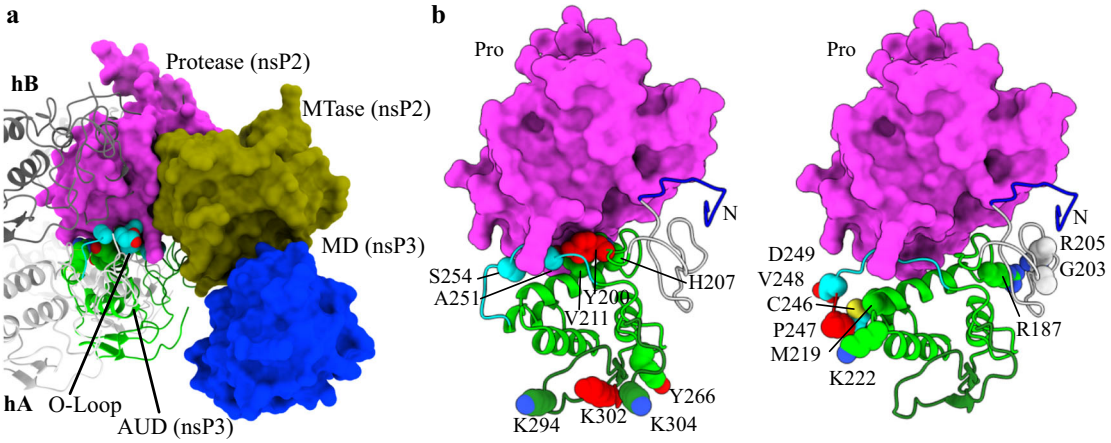

Fig. 3 | Blockage of the AUD oligomerization interfaces in the non-cleaved nsP3 polyprotein. a Superposition of the Alphafold2 predicted structure of the uncleaved nsP2-3 on the nsP3 HSs. One turn of the helical scaffold is shown in dark and light gray cartoon (for hA and hB respectively). The model is superposed in the hA AUD of the helix. It is shown with nsP2 protease surface colored in magenta, the MTase domain in olive green, the nsP3 MD domain in blue and the AUD in green cartoons. The protease domain completely blocks the axial contacts of the helical scaffold in the nsP2-3 uncleaved protein structure. **b** Same structure than in (**a**), showing only the protease domain and the AUD domain. On the left panel the residues mediating axial interactions shown in Fig. 1g are shown in spheres and colored according to panel a. On the right panel we have the same representation for the lateral contacts. The residues mutated in the replicon experiments (Y200A, P247A/V248A and K302A) are colored in red and labeled (see section "Mutations on the nsP3 AUD oligomerization interfaces affect RNA synthesis and production of structural proteins"). Only the Y200A is in the interface between the nsP2 protease and the AUD. The N terminus of the AUD connecting with the macrodomain is colored in blue.

long aggregates and weak formation of scaffolds, respectively, when compared to the WT nsP3 (Fig. 7c). In agreement with the observations in cells, the nsP3 Y200A mutant was unable to form tubes in vitro (Fig. 7c, Supplementary Fig. 10a). This is consistent with the central role of Y200 in the H bond network nailing the interprotomer axial interface as revealed by the structure (Fig. 1g).

Mutations on the nsP3 AUD oligomerization interfaces affect RNA synthesis and production of structural proteins

To assess the role nsP3 HSs during viral infection, we introduced the most disruptive AUD mutations (Y200A, P247A/V248A and K302A/V303A) in a full length CHIKV molecular clone. In vitro transcribed viral RNAs were transfected into 293T or U2OS cells and infectious particle release in the supernatants was quantified by plaque assays (Fig. 7d, e, Supplementary Fig. 10b, c). The CHIKV K302A/V303A or P247A/V248A RNAs were severely impaired in viral particle production, while the CHIKV Y200A RNA did not produce any detectable infectious viruses (Fig. 7d, e, Supplementary Fig. 10b, c). Of note, some smaller plaques could be detected in CHIKV K302/V303A and P247A/V248A, reflecting a drastic negative effect of these mutations on infection spread. Similar results were obtained when the Y200A and P247A/V248A mutations were introduced in a WT SINV molecular clone (Fig. 7f). Comparison of the extracellular and intracellular amounts of infectious viruses in U2OS cells expressing K302A/V303A, P247A/V248A and Y200A mutant RNAs revealed a similar reduction of viral particle production (Fig. 7d, e, Supplementary Fig. 10d). This suggests that the decrease in progeny infectious particle production results from a default in infectious particles assembly rather than in particle release. We then analyzed the effects of nsP3 AUD mutations on CHIKV RNA synthesis by introducing the Y200A, K302A/V303A and P247A/V248A mutations in a CHIKV sub-genomic replicon containing a dual luciferase (Luc) reporter[13]. In this construct, the Renilla Luc (Rluc) is expressed as a C-terminal fusion with nsP3 and the firefly Luc (FLuc) replaces the structural proteins. Rluc is produced following translation of both the input and nascent RNA genomes, while FLuc is expressed from the sub-genomic promoter only when sgRNA replication occurs. We used as control a CHIKV replicon containing the GDD-to-GAA mutation in the nsP4 catalytic site[24], which abolishes viral RNA synthesis but not the initial translation of nsPs. The Y200A mutant phenocopied the GAA mutant as it failed to form dsRNA foci (Supplementary Fig. 10e) and had a total defect in viral replication (Fig. 7g). The K302A/V303A and P247A/V248A are translated and produced RLuc, indicating that viral genomic RNA replication occurs, although at lower level (1.7-fold at 48 h after transfection) when compared to the WT replicon (Fig. 7g). In contrast, the FLuc activity was significantly reduced in viruses harboring the K302A/V303A and P247A/V248A mutations (11- and 28-fold respectively at 48 h after transfection). This suggests that the K302A/V303A and P247A/V248A mutations may result in a drop of production of structural proteins that consequently could explain their major defect in infectious virus particle release. This is consistent with a study showing that P247A/V248A mutation has a deleterious effect on the ability of CHIKV to produce sgRNA[13]. However, we cannot rule out the possibility that K302A/V303A and P247A/V248A mutations may impact additional steps in the alphavirus life cycle such as in nucleocapsid formation and/or virus assembly. Altogether our results showed that nsP3 scaffolds are critical for alphavirus infection.

Discussion

In this study, we show that CHIKV nsP3 auto-assembles via its AUD into tubular scaffolds present both in mature vRCs and alpha-granules. The AUD appears to play a role in different functional states of the vRC required for negative and positive vRNA synthesis and, later on infection, the formation of alpha-granules (Fig. 8). At this step, AUD oligomerization is likely blocked by the protease domain of nsP2. Only one mutant (Y200A) abrogated the overall synthesis of RNA. Y200A is the only mutation capable of both interfere the scaffold formation and the interaction with the protease in the uncleaved polyprotein. In consequence, the mutation could be affecting the function of the early uncleaved RC. A conformational change of the vRC would be necessary to release the O-loop, allowing nsP3 assembly on mature (crowned) vRCs after proteolytic cleavage. Mutants partially disrupting nsP3 assemblies (i.e. P247A/V248A and K302A/V303A mutations) would prevent the crowns to be fully functional, resulting in the reduction of sgRNA synthesis (Fig. 8). As infection progresses, CHIKV nsP3

https://doi.org/10.1038/s41467-024-51952-z

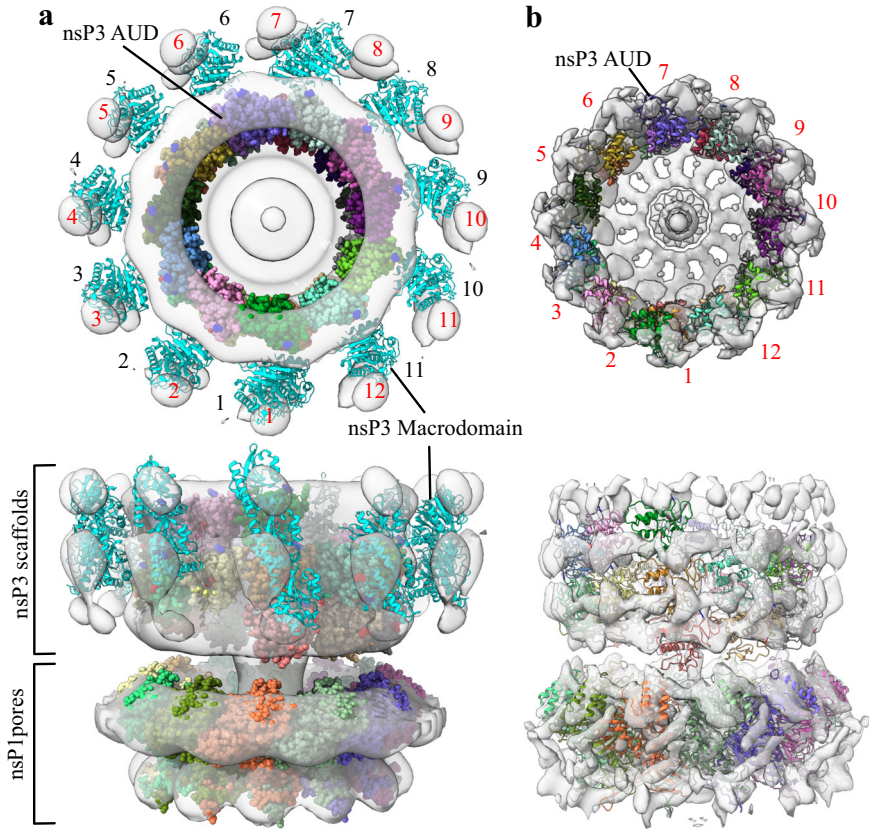

Fig. 4 | Superposition of nsP3 HSs on tomographic reconstructions of membrane-associated CHIKV RCs. a Superposition of nsP1 capping pores and the nsP3 scaffolds on the tomographic reconstruction of CHIKV RCs. Top and lateral views are shown in the top and bottom panels respectively. The volume is shown as a transparent gray surface. nsP1 and nsP3 AUDs are colored by protomer and shown in spheres, the MDs of nsP3 are shown in cartoon and colored in cyan. Their position with respect to the AUDs was determined based on their fitting on the map shown in Fig. 1b (EMD: 17730). The tomographic volume was calculated applying a 12-fold symmetry and consequently has 12 outer volumes on the region which are shown numbered[8]. The superposition shows the consistent matching in size and shape of AUD helices with the rings above the nsP1 capping pores and the outer spherical volumes have a partial matching with the MDs positions found in HSs. However, the structure of the nsP3 helical scaffold have 11,37 protomers per turn instead of 12, slightly breaking the symmetry with the nsP1 pores and the volume reconstructions. Superposition allows to confidently assign the central ring above nsP1 to the AUDs and the peripheral volumes to the MDs. **b** same representation of the superposition of capping pores and nsP3 scaffolds on the volume of RCs reported by Tan et al.[9]. The volume reaches higher resolution and only shows electron density for the AUD region of the nsP3 scaffold. The volume was also calculated imposing C-12 symmetry.

accumulates into alpha-granules organized by highly-ordered networks of helical tubular scaffolds that contain host factors, genomic RNA and viral capsid proteins. NsP3 is not essential for viral particle assembly[25]. However, one can speculate that alpha-granules may control the homeostasis of vRNA and capsid protein accessible pools in the infected cell and indirectly influence viral assembly. However, since nsP3 HSs are present in both RCs and alpha-granules, we cannot assess in our experiments if mutations perturbing HS formation have an effect on particle assembly or vRNA translation. The inner architecture of alpha-granules also challenges our current understanding of the structural organization of non-membranous organelles by combining both intrinsically disordered regions and highly ordered scaffolds. There is no precedent for such assemblies of non-structural proteins among positive-strand RNA viruses. Macromolecular structures have been reported for non-structural proteins of segmented negative strand RNA viruses such as the NSm and NSs of Bunyamwera and Rift Valley Fever bunyaviruses, respectively[26,27]. Helical macrostructures are also found in the nucleocapsids of Mononegavirales[28]. Interestingly, Ebola viruses incorporate in the replicating nucleocapsids the Vp35 protein which interacts with G3BP to prevent stress granule formation[29].

NsP3 protein assemblies represent a pivotal element involved in both the replication complex and in alphagranule assemblies. The structural characterization of the full replication complex in different conformational−functional states will be required for the full understanding of the exact role of nsP3 on regulating the polymerase function and the transition between early and late replication complexes. In another hand, for a clearer view of the exact role of alphagranules for infection, the reconstruction of larger assemblies by incorporating host factors and viral RNA will be paramount. Altogether these findings will hopefully permit to design structure-based mutants allowing to decouple the nsP3 function in the RC from its functional role in alphagranules. More generally speaking, further studies of other viral and non-viral biomolecular condensates will reveal if the architecture of alpha-granules is specific feature of alphavirus or a more extended trend.

Methods

Recombinant expression and purification of CHIKV nsP3 protein

NsP3 was expressed in Hi5™ cells (Thermo Fisher) using BactoBac system (Thermo Fisher). The coding sequence of CHIKV nsP3 (corresponding to residues 1334-1863 of the non-structural polyprotein sequence from the S27 African prototype (Uniprot ID Q8JUX6) was synthesized by Gen9 as a codon optimized gene and subcloned into a pFastBac vector (Thermo Fisher) with a C-terminal hexahistidine tag). The same constructs based on the alignment of Supplementary Fig. 6

https://doi.org/10.1038/s41467-024-51952-z

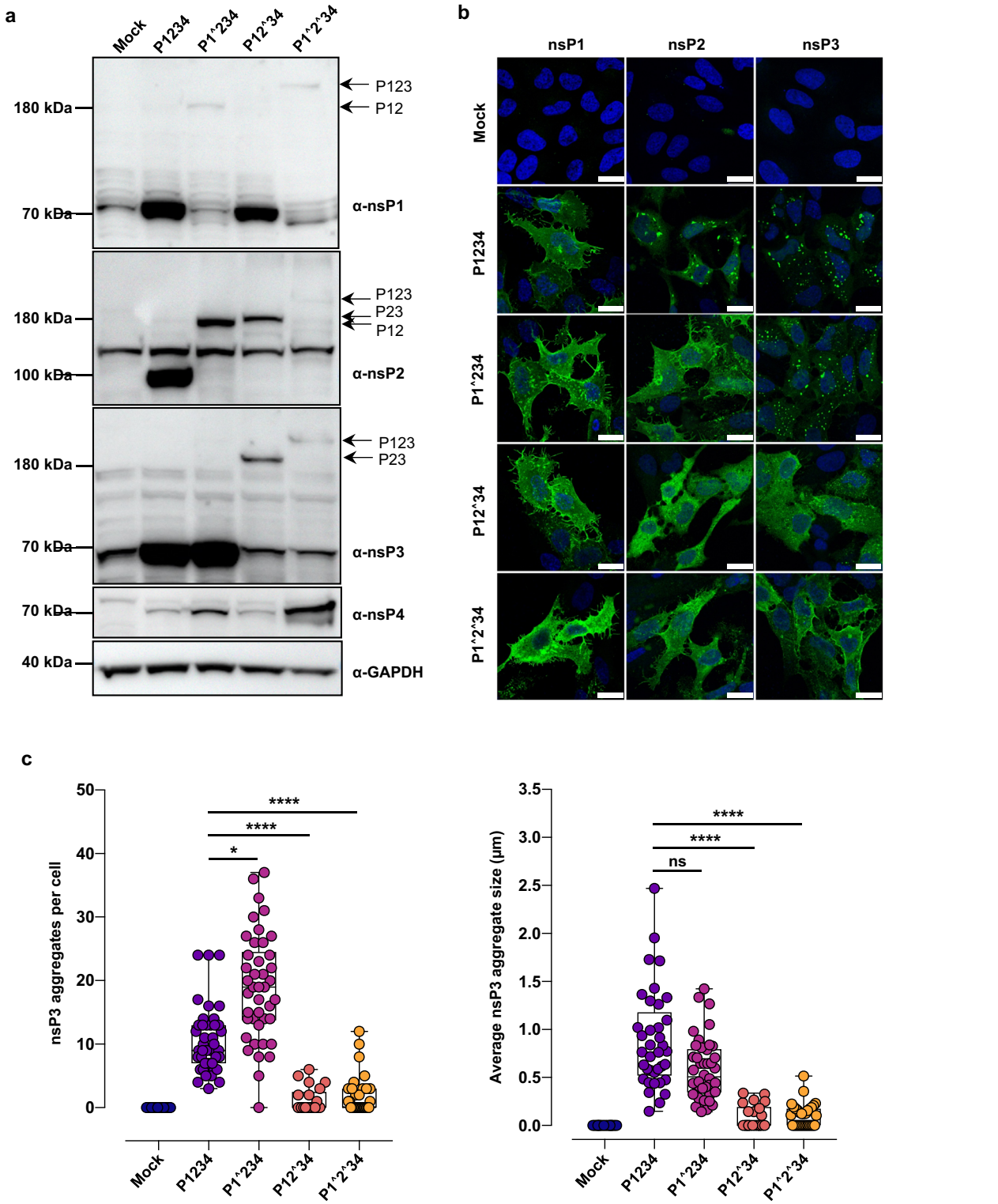

Fig. 5 | NsP3 HS formation requires nsP2-nsp3 precursor cleavage. a–**c** U2OS cells were transfected with a plasmid encoding the polyprotein precursor (P1234) or cleavage-deficient mutants (^ indicates the uncleavable sites). **a** Cell lysates were separated by SDS-PAGE and non-structural proteins processing was ascertained by immunoblot analysis with nsP1, nsP2, nsP3, nsP4 or GAPDH antibodies. **b** The subcellular localization of nsP1, nsP2 and nsP3 was assessed by immunofluorescence at 48 h post-transfection. **a**, **b** Data shown are representative of 2 independent experiments. **c** Graph bar showing the number of nsP3 aggregates per cell (left) and the average aggregate size (right) from two independent biological replicates ($n = 20$ cells in mock, $n = 43$ cells for P1234, $n = 42$ cells in P1^234, $n = 21$ cells in P12 ^ 34 and $n = 31$ cells in P1 ^ 2 ^ 34). Data are presented as mean value ± SD and adjusted *P*-values are calculated by one-way ANOVA with Kruskal-Wallis multiple comparisons test. Significant differences denoted by ****$P < 0.0001$, * $P = 0.0232$. Source data are provided in the Source Data file.

https://doi.org/10.1038/s41467-024-51952-z

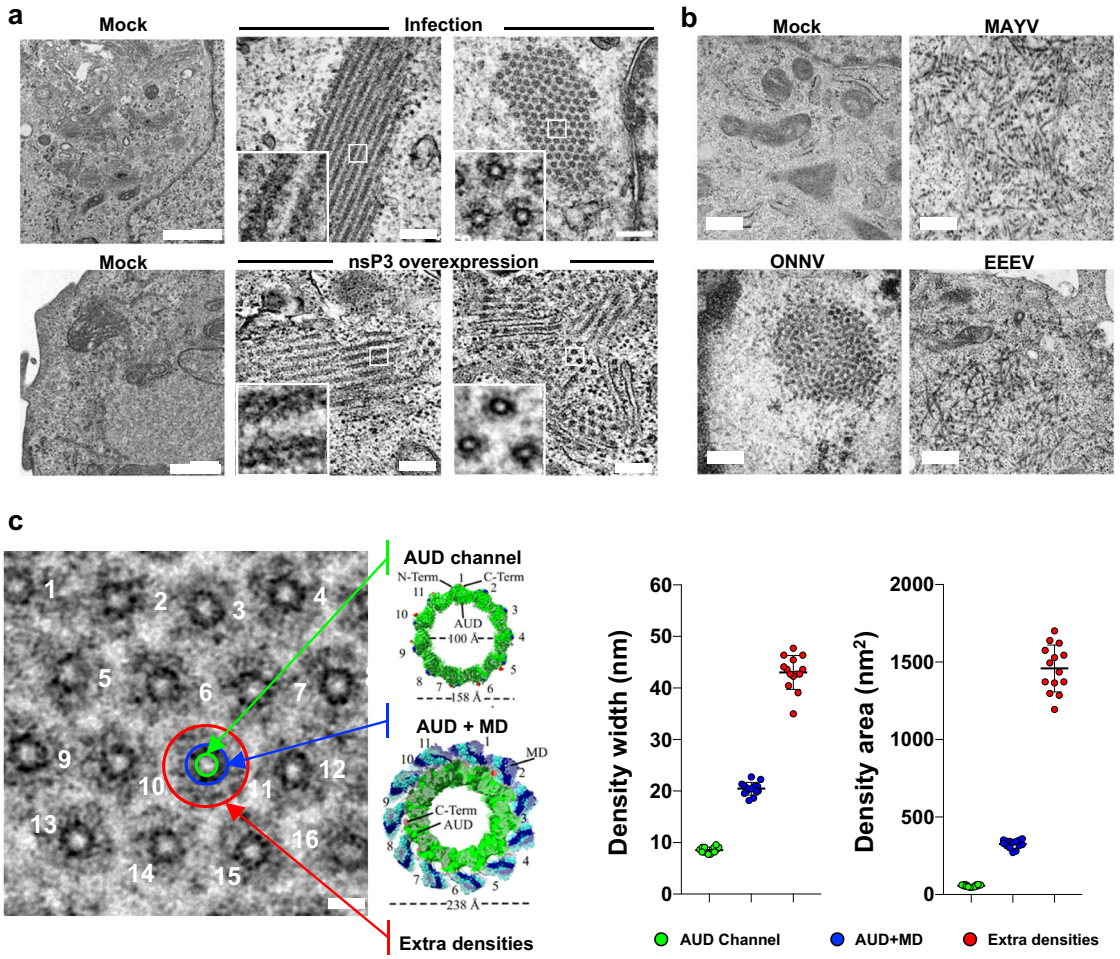

were produced for EEEV and SINV (Uniprot ID Q4QXJ8 and P27283 respectively) with genes synthesized by TWIST. Site directed mutagenesis was performed on the pFB-nsP3 construct by Q5 Site-Directed Mutagenesis Kit Quick Protocol (NEB) and the whole nsP3 sequence was verified by sanger sequencing. Recombinant bacmids and viruses were produced in YFP-DH10 Bac cells and Sf21 cells, respectively according to the manufacturer's protocols (Thermo Fisher). For protein expression, Hi5 cells were grown in suspension at a density of 0.5–1.0 × 10^6 ml^{-1} and then infected with baculoviruses at 2% volume of the culture. Cells were harvested at day 2–3 post cell arrest. Cells were resuspended in buffer A (20 mM Tris pH 8, 500 mM NaCl, 2 mM TCEP, 5% glycerol, 20 mM imidazole) supplemented with 2 mM PMSF,

Fig. 6 | CHIKV nsP3 assembles into tubular structures that define the architecture of alpha-granules. a Transmission electron microscopy of human fibroblasts infected with CHIKV 21 strain (MOI of 10) for 24 h (upper panel) or stably expressing the CHIKV nsP3 (lower panel). Longitudinal (left) and transversal (right) views of the nsP3 tubes are shown. Images are representative of two independent experiments. Scale bars, 500 nm (mock panels) and 200 nm (infection and nsP3-overexpression panels). **b** Transmission electron microscopy of human fibroblasts transfected with empty plasmid (mock) or MAYV, OONV or EEEV nsP3 plasmids. Scale bars, 500 nm. **c** The left panel shows a micrograph corresponding to a section of alpha granules perpendicularly cutting a bundle of HSs. A 0.2 μm^2 is depicted. 16 HSs are present and numbered within the 0.2 μm^2 square. The scaffold numbered as 13 is superposed to three concentric circles of the dimensions obtained for the HSs (see Fig. 1) including the internal channel (green circle), the MDs (blue circle), the and external density around the tube (red circle). Circles diameter and area were calculated with ImageJ for each one of the 16 HSs in the image (bottom panels). Scale bar, 20 nm. Data are presented as mean ± SD from one experiment. Source data are provided as a Source Data file. **d** Human fibroblasts were infected with CHIKV 21 strain for 24 h. Cells were immunostained with an anti-Capsid or anti-nsP3 specific Ab. Viral genomic RNA was detected using a CHIKV-genome specific fluorescent RNA probes. Co-localization analysis was performed using JACoP plugin implemented in ImageJ[37]. Scale bars, 20 μm. Images are representative of 2 independent experiments.

10 μg/ml DNAse and 5 mM $MgSO_4$, and lysed by sonication. Lysates were centrifuged at 18,000 g for 1 h to remove unbroken cells and debris. The clarified lysate was incubated with Ni-NTA resin (GE Healthcare) in batch at 4°C for 30 min. Resin was washed with 10 column volumes of lysis buffer and the protein eluted over 1.5 column volumes with buffer A containing 500 mM imidazole. Elution fractions containing the protein were pooled and concentrated (Amicon 30k MW C/O) for size exclusion chromatography. Samples were applied to a Supedex 200 10/300 increase column (GE Healthcare) pre-equilibrated with the size exclusion buffer: 20 mM HEPES pH = 8.0; 500 mM NaCl; 5% glycerol and 2 mM TCEP.

Grid preparation for cryo-EM imaging

Quantifoil grids R2/1 were treated with plasma glow discharge (Quorum) two times for 25 s at 15 mA with a 2 min pause between the pulses. 3.5 μl of Purified nsP3 protein at 1 mg/ml in freezing buffer (100 mM NaCl, 20 mM HEPES pH7.5 and 2 mM TCEP) were applied on the prepared grids and left to incubate for 1 min for binding at RT. The grid was transferred in Leica GP plunge freezer and then blotted for 10 s from the back side. Grids were plunged into liquid ethane and then transferred and stored in liquid nitrogen until the imaging session. For data collection on nsP3 grids we used the Titan Krios microscope in ESRF CM01 beamline[30] at Grenoble, France. Vitrified nsP3 grids were loaded into the microscope equipped with a Gatan K3 direct electron detector and a Gatan Bioquantum LS/967 energy filter. Cryo-EM data were acquired with EPU software (FEI) at a nominal magnification of ×81,000, with a pixel size of 1.06 Å and a total dose of 42 e/$Å^2$ (see Table 1). 13,046 image frames were acquired in super-resolution mode with a flux of 18.1 electrons per square-pixel, fractionated into 40 frames with a defocus range from −0.6 μm to −2.6 μm. Using the CM01 real-time processing setup, within the SCIPION wrapper[31], the imported movies were drift-corrected using MotionCor2 and CTF parameters were estimated using Gctf for real-time evaluation. Further data processing was conducted using the cryoSPARC suite[32] and Relion4.

Cryo-EM image processing

13,046 motion-corrected and dose-weighted micrographs were imported into cryoSPARC for further processing and CTF estimated. After exposure curation 12809 micrographs remained. Combining manual picking plus two rounds of 2D classification template picking we obtained an initial set of templates for template-based filament tracing. Filament tracing was performed with a segment diameter of 130 Å and a distance of 32.5 Å based on measurements within 2D classes and resulted in 6,283,414 particle images. Subsequent picking inspection (NCC score > 0.180, local power 83.0-108.0, curvature, 0.0012 (1/ Å) and sinuosity < 1.18) reduced the selection to 831,539 particles (5,451,875 particles excluded). 807,973 particles were extracted with an extraction crop size of 408 pixels and 2D-classified into 200 classes. Helical refinement without prior estimation of helical twist and helical rise was not successful. Accordingly, helical twist and rise estimates were found by power spectrum analysis in helixplorer software (https://rico.ibs.fr/helixplorer/helixplorer/ see supplementary information). Helical parameters were refined during 3D reconstruction and converged to a twist of -164.175 degrees and a helical rise of 2.782 Å. The map refined to a nominal 2.52 Å resolution (according to 0.143 threshold) and a B-factor of 106.0 (EMD: 17729). Symmetry expansion (Point group symmetry: C1, helical twist (degrees)): -164.175, helical rise (Å): 2.782, helical symmetry order: 12 of all final particles in this map was performed. Symmetry expanded particles (9,695,676 particles) were used in local refinement with a local mask covering an 3 × 3 array of 9 helical domains and a protruding central domain to cover the potential macrodomain resulted in a map of a nominal 2.36 Å resolution and slightly improved side chains (EMD: 17678).

807,973 non-subtracted particles and reference maps from cryoSPARC were imported from cryosparc into Relion. A first round of unmasked refinement was performed followed by masked refinement giving rise to better defined protruding densities of the potential macrodomain (EMD: 17730). For that a cylindrical mask covering the 30% central section of the helix and the protruding densities was designed from the helix. Different sets of masked 3D classification variants were tested (varying class size, with and without alignment, with and without particle subtraction). Here a smaller mask covering only a threefold array of two neighboring AUD and the protruding density was used. The best class was derived from non-particle subtracted classification into 3 classes (supplementary map in EMD: 17730).

Model building, refinement and analysis

The first model of the whole nsP3 was obtained using ColabFold[33] (see supplementary information). The predicted model AUD domain fitted perfectly in the maps with the exception of the O loop which was traced by hand using Coot. A model with five AUD including one protomer and four neighbor contacting protomers was done using Coot and real-space refined using Phenix on the 2,35 Å resolution map (PDB: 8PHZ and EMD: 17678 respectively). The HVD and MD conformations predicted by Alphafold2 where incompatible with the helix formation, in consequence for the interpretation of the MD densities at low resolution the MD was placed manually and fitted into density using ChimeraX. The biological assembly with 120 protomers forming the helix was calculated extending the helical symmetry with ChimeraX setting an axial rise of 2.782 Å and a helical twist of −164.175° on the helical reconstruction map at 2.53 Å resolution (PDB: 8PK7, EMD: 17729). For the analysis of interprotomer contacts we used the PISA server (https://www.ebi.ac.uk/pdbe/pisa/). We applied a cutoff of 3.5 Å for assigning H bonds as indicated in Supplementary Fig. 6.

Cell culture

HEK293T (ATCC, CRL-3216), Vero E6 (gift of Marc Lecuit, Pasteur Institute Paris, France), BHK-21 (ATCC, CCL-10) and U2OS cells (gift of Andres Merits, University of Tartu, Estonia) were cultured in DMEM supplemented with 10% FBS, 1% penicillin–streptomycin, and 25 mM HEPES. Fibroblast BJ-5ta cells (ATCC, CRL-4001) were cultured in DMEM supplemented with 20% Gibco Media 199, 10% FBS, 1% penicillin–streptomycin, 25 mM HEPES and 10 μg/mL Hygromycin D.

https://doi.org/10.1038/s41467-024-51952-z

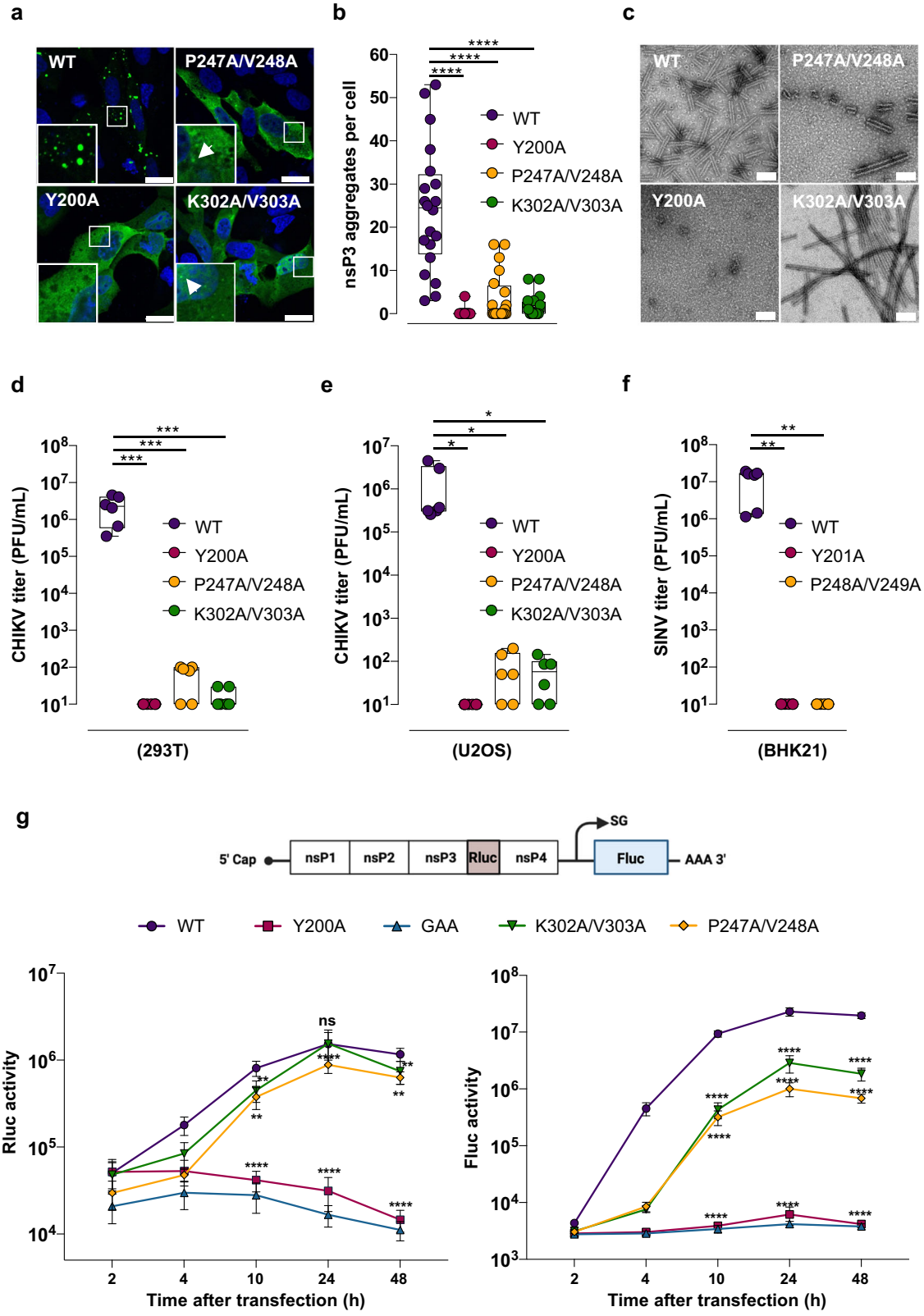

All cell lines were cultured at 37 °C in 5% CO2. All cell lines were routinely tested to be free of mycoplasma contamination.

Virus strains and production

CHIKV-21 (strain 06-21 from Reunion Island) was previously described[34] and obtained from Philippe Despres (Institut Pasteur, Paris, France). CHIKV West Africa (strain 37997), CHIKV St Martin (H20235 2013 Asian), MAYV (strain TC 625) and ONNV (strain Dakar 234) were obtained from the European Virus Archive (EVA) collection. Viruses were propagated with limited passages on Vero E6 cells. CHIKV 181/25 molecular clone (gift from Dr Gofinnet Christine, Institute of Virology Charité, Berlin, Germany) was derived from the parental Asian strain AF155561 and attenuated by two amino acid substitutions in the E2 glycoprotein[35]. Recombinant CHIKV

Fig. 7 | nsP3 helical scaffolds are required for CHIKV infection. **a**–**c** Characterization of nsP3 AUD mutants. U2OS cells were transfected with plasmids encoding FLAG-tagged wild-type CHIKV nsP3 or mutants harboring substitutions of amino acids involved in AUD-AUD contacts (Y200A, P247A/V248A, and K302A/V303A). **a** At 48 h after transfection, cells were fixed and nsP3 sub-cellular localization was assessed by immunofluorescence using an anti-FLAG mAb. Images were acquired by confocal microscopy and are representative of 2 independent experiments. White arrows indicate the presence of nsP3 aggregates. Scale bars, 20 µm. **b** The number of nsP3 aggregates per cell was assessed using ImageJ. Data are presented as min to max with all data points shown ($n = 20$ cells for each condition). Adjusted *P*-values are calculated by one-way ANOVA with Dunnett's multiple comparison test (****$P < 0.0001$). **c** Negative staining micrographs of nsP3 in vitro assembly experiments after incubation at 0.1 M NaCl for 1 h showing the assembly of HSs. White scale bars are 100 nm long. **a**–**c** Data are representative of 2 independent experiments. **d**, **e** HEK293T (**d**) or U2OS (**e**) cells were transfected with the indicated in vitro-transcribed and capped CHIKV RNA. Viral titers in the supernatants were quantified by plaque assays 48 h after RNA transfection. **f** HEK293T were transfected with the indicated in vitro-transcribed and capped SINV RNA. Viral titers in the supernatants were quantified by plaque assays 48 h after RNA transfection. Data in (**d**–**f**) are presented as min to max with all data points shown ($n = 3$ independent experiments performed in duplicate). Adjusted *P*-values are calculated by one-way ANOVA with Dunnett's multiple comparison test (***$P = 0.0003$). **g** 293 T were transfected with CHIKV-D-Luc-SGR wild type (WT) and the indicated mutant RNA and harvested for both RLuc and Fluc assays at the indicated times. GAA: inactive mutant of nsP4 polymerase. Data are presented as mean value ± SD ($n = 3$ independent experiments performed in quadruplicate) and adjusted *P*-values are calculated by two-way ANOVA with a Dunnett's multiple comparison test (****$P < 0.0001$). Source data are provided as a Source Data file.

nsP3-mCherry and CHIKV-Rluc molecular clones were derived from CHIKV isolate obtained during the Mauritius outbreak in 2006 (GenBank accession no. FJ959103)[36]. To generate infectious viruses from CHIKV molecular clones, capped viral RNAs were generated from the NotI-linearized CHIKV plasmids using a mMESSAGE mMACHINE SP6 or T7 Transcription Kit (Thermo Fischer Scientific) according to manufacturer's instructions. Resulting RNAs were purified by phenol:chloroform extraction and isopropanol precipitation, resuspended in water, aliquoted and stored at −80 °C until used. Thirty µg of purified RNAs were transfected in BHK21 with lipofectamine 3000 reagent and supernatants harvested 72 h later were used for viral propagation on Vero E6 cells.

All virus stocks were purified through a 20% sucrose cushion by ultracentrifugation at 80,000 g for 2 h at 4 °C. Pellets were resuspended in HNE1X pH7.4 (Hepes 5 mM, NaCl 150 mM, EDTA 0.1 mM), aliquoted and stored at −80 °C. Viral titers were determined on Vero E6 cell by plaque assay and are expressed as PFU per mL and also by flow cytometry as previously described[14]. Briefly, Vero E6 cells were incubated for 1 h with 100 µL of 10-fold serial dilutions of viral stocks. The inoculum was then replaced with 500 µL of culture medium and the percent of E2 expressing cells was quantified by flow cytometry at 8 hpi. Virus titers were calculated using the following formula and expressed as FACS Infectious Units (FIU) per mL. [Titer (FIU/mL) = (average % of infection) x (number of cells in well) x (dilution factor) / (mL of inoculum added to cells)].

Plasmid constructions

All N-terminal FLAG-tagged full-length nsP3 constructs derived from CHIKV Sri Lanka/2006/SL15649 strain (Accession number: MK028838.1), the nsP3 macrodomain (MD; aa A1-T160), the alphavirus unique domain (AUD; aa Q161-Y324) and the hypervariable domain (HVD; aa R325-L523) were synthesized and cloned into pcDNA 3.1 (-) mammalian expression vector by GenScript. The WT FLAG-tagged nsP3 and FLAG-tagged AUD constructs were subcloned into a pLVX-EF1a-IRES-puromycin (Takara) using NotI and BamHI restriction enzymes. pMC-GTU CHIKV P1234 WT and mutant replicase plasmids were described elsewhere[19] and kindly provided by Pr. Andres Merits (University of Tartu, Estonia). FLAG-tag ONNV-nsP3 (isolate UVRI0804, accession number: ON595759.1), FLAG-tag MAYV-nsP3 (isolate Haiti-1/2014, accession number: KY985361.1), FLAG-tag SINV (Toto1) and FLAG-tag EEEV-nsP3 (isolate USA/R131399b/2019, accession number: MT782295.1) were synthesized and cloned into pcDNA 3.1 (-) mammalian expression vector by GenScript.

To establish pCHIKV with an Rluc gene insertion in the nsP3 gene (briefly pCHIKV-Rluc), three PCR fragments were amplified first. A DNA sequence encoding part of CHIKV nsp3 was amplified from pCHIKV-M[36] using primers 5009 F (5′-TGACCACAACGTGCCATCGCG-3′) and Bo426 (5′ CGGGGTCGTACACCTTGGAAGCCATCAAGCTTTCGATTTCTCCTTCGTTG-3′). Second, the Rluc gene was amplified from phRL-CMV (Promega) using primers Bo425 (5′-CAACGAAGGAGAAATCGAAAGCTTGATGGCTTCCAAGGTGTACGACCCCG-3′) and Bo428 (5′-CCGAAAGTTAGTAGCTCAGAAGATAGTGACTCCTGCTCGTTCTTCAGCAC-3′). Third, a CHIKV sequence encoding parts of nsP3 and nsP4 derived from pCHIKV-M were amplified using Bo427 (5′-GTGCTGAAGAACGAGCAGGAGTCACTATCTTCTGAGCTACTAACTTTCGG-3′) and Bo409 (5′-GACTTCCTCCAGGGTGTTCACC-3′). After fusing all fragments in a fusion PCR reaction using the outer primer pairs 5009 F and Bo409, the resulting fragment was cut with NheI and AgeI and fused together with an NgoMIV-NheI derived fragment of pCHIKV-M into pCHIKV-M cut with a NgoMIV-AgeI. To establish the pCHIKV-Rluc mutant Y200A, two PCR fragments were amplified from pCHIKV-Rluc using primers Bo408 (CACCACGTGCTCCTGGTCAGTG) and Bo1646 (5′-TCCCTTCTAGAGCTGAGTACAGTG -3′) or Bo1645 (5′-CACTGTACTCAGCTCTAGAAGGGA-3′) and Bo409 (see above), respectively. The resulting fragments were fused via PCR amplification using the outer primers Bo408 and Bo409. For the other two mutants, PCR fragments were amplified and fused accordingly except that the complementary primers encompassing the mutations were replaced by Bo1651 (5′-GGCAGAAATGCGCTGCTGATGATGCAGA-3′) and Bo1652 (5′-TCTGCATCATCAGCAGCGCATTTCTGCC-3′) for the P247A/V248A mutant or Bo1654 (5′-TTAGAGCATTTTGCTGCTTGCACTCCTT-3′) and Bo1653 (5′-ACGCATCATCTGCACCCAAAACTGT-3′) for the K302A/K303A mutant, respectively. The resulting PCR fragments were cut with SacII and AgeI and inserted together with a BamHI-SacII derived fragment from pCHIKV-Rluc into pCHIKV-Rluc cut with BamHI and AgeI.

The other two mutants were obtained accordingly, except that the complementary primers encompassing the mutations were replaced by Bo1651 (5′-GGCAGAAATGCGCTGCTGATGATGCAGA-3′) and Bo1652 (5′-TCTGCATCATCAGCAGCGCATTTCTGCC-3′) for the P247A/V248A mutant or Bo1654 (5′-TTAGAGCATTTTGCTGCTTGCACTCCTT-3′) and Bo1653 (5′-ACGCATCATCTGCACCCAAAACTGT-3′) for the K302A/K303A mutant, respectively.

To establish a SINV clone expressing Gaussia luciferase (GLuc) under a second subgenomic promoter, a GLuc cassette was amplified from a CHIKV-sgGLuc clone kindly provided by Andres Merits using primers Bo702 (5′-CTGACTAATACTACAACACCACCACCgggcccACCATGGGAGTCAAAGTTCTGTTTGCCC-3′) and Bo705 (5′-CTCAATGCCAGTAGGACAGGTGTAATgtttaaacTTAGTCACCACCGGCCCCCTTGATC-3′). In addition, the region upstream of the GLuc insertion site was amplified from pSINV (Toto1101, kindly provided by Charles M. Rice) using primers Bo701 (5′-GTACTGGAGACGGATATCGCATC-3′) and Bo703 (5′-GGGCAAACAGAACTTTGACTCCCATGGTgggcccGGTGGTGGTGTTGTAGTATTAGTCAG-3′). The region downstream of the GLuc insertion site was amplified from pSINV using primers Bo704 (5′-GATCAAGGGGGCCGGTGGTGACTAAgtttaaacATTACACCTGTCCTACTGGCATTGAG-3′) and Bo706 (5′-ACTCCATGTCGTATGCTGACGAC-3′). All three fragments were fused together with the outer primers Bo701 and Bo706. The resulting fragment was cut with SapI and AatII and cloned into pSINV cut with the same restriction enzymes to yield pSINV-sgGluc (SG83).

https://doi.org/10.1038/s41467-024-51952-z

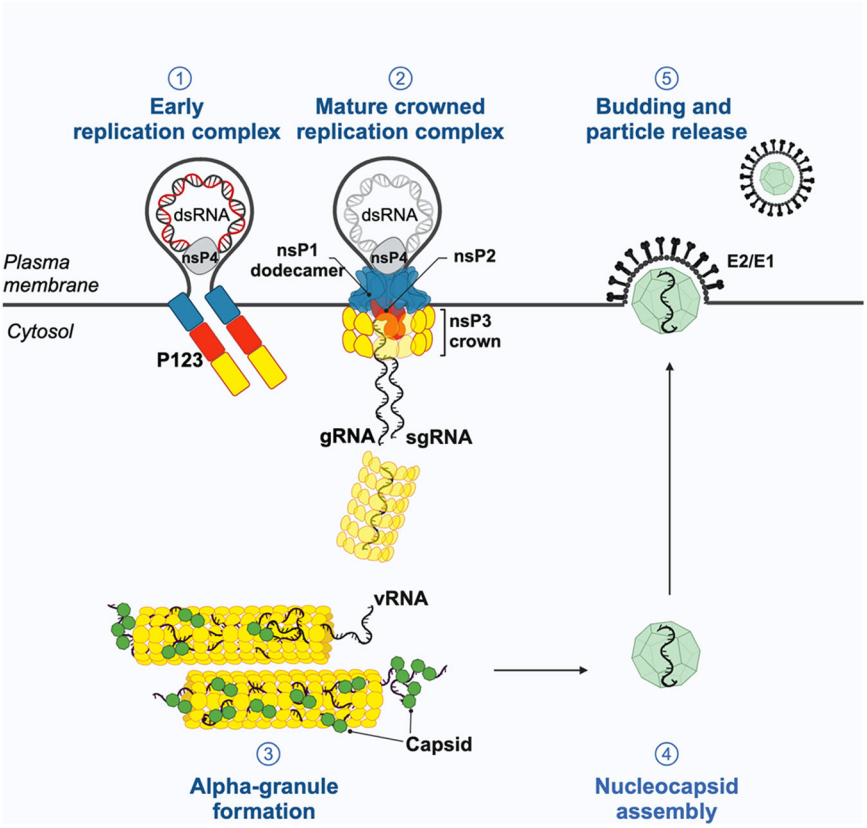

Fig. 8 | Model of the role of nsP3 HSs during the alphavirus infection. 1 After vRNA release in the cytoplasm, the P1234 polyprotein is processed into P123 + 4, forming the early vRC and spherules that house the dsRNA intermediate. Axial contacts between adjacent AUD promoters trigger the formation of a helical scaffold (HSs) required for dsRNA synthesis. **2** A conformational change switch concomitant to the processing of the P123 by nsP2 releases the AUD loop and mediates nsP3 oligomerization and subsequent cytoplasmic crown formation, leading to the mature vRC synthesizing positive gRNAs and sgRNAs. **3** As infection progresses, nsP3 accumulates into alpha-granules organized by highly-ordered networks of helical tubular scaffolds. **4** Because these structures contain vRNA and capsid, nsP3 assemblies may sort the vRNA and deliver it in the cytoplasm for structural protein synthesis and/or nucleocapsid assembly. **5** Once the nucleocapsid reaches the plasma-membrane, the capsid/E2/E1 envelop protein interaction triggers an organized budding event leading to the release of infectious viral particles.

To establish the pSINV-sgGLuc nsP3 mutant Y201A (BK857), two PCR fragments were amplified from pSINV-sgGluc using primers Bo1829 (5′-GCGTTGCACACAGCCAGTTAC-3′) and Bo1831 (5′-ggtgcctt cgaaGgcCGAATACAATTT-3′) or Bo1830 (5′-AAATTGTATTCGgcC ttcgaaggcacc-3′) and Bo1836 (5′-TTAGCCTTGGCGGTGGAATAGG-3′), respectively. The resulting fragments were fused via PCR amplification using the outer primers Bo1829 and Bo1836. For the P248A/V249A mutant, PCR fragments were amplified and fused accordingly, except that the complementary primers encompassing the mutations were replaced by Bo1833 (5′-CGGGTTATGGTCAGcAgCgcacttttcgcg-3′) and Bo1832 (5′-cgcgaaaagtgcGcTgCTGACCATAACCCG-3′) (BK858)). The obtained PCR fragments were cut with ClaI and SpeI and inserted into pSINV-sgGluc also restricted with ClaI and SpeI to obtain the respective SINV mutant.

Replicons and dual luciferase assays

The AUD mutant Y200A, K302AK303A, and P247AV248A were introduced in the CHIKV replicon CHIKV-D-LucSGR[13](provided by Pr Mark Harris) by site-directed mutagenesis (Thermo Fisher, Phusion Site-Directed Mutagenesis Kit 20 RXNS). Capped RNA were generated from the CHIKV-D_luc SGR for transfection using the mMACHINE SP6 transcription kit (Thermo Fisher Scientific). 0.5 μg of CHIKV-D_luc SGR were transfected into cells using Lipofectamine 2000 as described by Gao et al.[13]. Both Renilla and Firefly Luciferase activity were measured using the Dual Luc assay system (Promega) according to the manufacturer's instructions. Each sample had a quadruplicate repeats and the data shown represented the mean of three experimental replicates ($n = 3$).

Lentiviral production

Lentiviral plasmids containing FLAG-tagged full-length nsP3 or AUD were packaged as previously described[14]. Supernatants were collected 48 h and 72 h after transfection, cleared by centrifugation (750 g for 10 min), filtered using a 0.45 μm filter and purified through a 20% sucrose cushion by ultracentrifugation (80,000 g for 2 h at 4 °C). Pellets were resuspended in HNE 1X pH 7.4, aliquoted and stored at −80 °C. Fibroblasts were transduced by spinoculation (750 g for 2 h at 33 °C) using these lentiviruses and selected with puromycin (2 μg/mL).

Antibodies

The following primary antibodies were used: anti-Flag M2 mouse monoclonal antibody (F1804, Sigma), anti-dsRNA J2 mouse monoclonal antibody (Scicons), anti-nsP1, anti-nsP2, anti-nsP3 and anti-Capsid rabbit polyclonal antibodies (in-house from Andres Merit's laboratory), anti-CHIKV E2 mouse monoclonal antibody (3E4), anti-GAPDH mouse monoclonal antibody (SC-47724, Santa Cruz Biotechnology), anti-FHL1 mouse monoclonal antibody (MAB5938, R&D Systems) and anti-G3BP1 mouse monoclonal antibody (H-10 sc-365338, Santa Cruz Biotechnology). The following secondary antibodies were used: Alexa Fluor 488-conjugated goat anti-rabbit IgG (A11034, Invitrogen), Alexa Fluor 488-conjugated goat anti-mouse IgG (A11001, Invitrogen), Alexa Fluor 647-conjugated donkey anti-rabbit IgG (A31573, Invitrogen), Alexa Fluor 647-conjugated donkey anti-mouse IgG (A31571, Invitrogen), Alexa Fluor 594-conjugated donkey anti-rabbit IgG (21207, Invitrogen), peroxydase-conjugated donkey

anti-rabbit IgG (711-035-152, Jackson ImmunoResearch), and anti-mouse/HRP (P0260, Dako Cytomotion).

Immunofluorescence

For nsP3 alpha-granule characterization in infectious context, human fibroblasts (10^4 cells per well) were grown on Lab-Tek CC2 chamber slides (Nunc) for 24 h. Cells were inoculated with CHIKV-21 or CHIKV nsP3-mCherry at the indicated MOIs. For immunofluorescence in the context of transient transfection, U2OS (3×10^5 cells) were grown on Lab-Tek CC2 chamber slides for 24 h. Cells were transfected with 250 ng of DNA expression plasmid using jetOPTIMUS® DNA Transfection Reagent (PolyPlus) according to the manufacturer's instructions. At 7 and 24 hpi, or after 48 h of transfection, cells were washed with PBS and fixed with 2% (v/v) of PFA diluted in PBS for 15 min at room temperature. Fixed cells were washed with PBS for 5 min, then incubated with 0.1 mM of glycine in PBS for 30 min at room temperature. Cells were permeabilized and blocked with 0.1% Triton X-100 and 3% (w/v) BSA in PBS for 45 min. Cells were incubated for 1 h at room temperature with primary antibodies, and washed with PBS. Cells were labeled with corresponding Alexa Fluor-conjugated secondary antibodies (1 µg.ml^{-1}) for 30 min at room temperature. All antibodies were diluted in PBS supplemented with 3% (w/v) BSA. Slides were mounted with ProLong Gold antifade reagent containing DAPI for nuclear staining (Thermo Fisher Scientific). Fluorescence microscopy images were acquired using a LSM 800 confocal microscope with the following objectives: Plan-Apochromat 63 x/1.40 Oil DIC M27 and Plan-Apochromat 40 x/1.3 Oil DIC (UV) VIS-IR M27 (Zeiss).

RNA-fluorescent in situ hybridization

A pool of 48 Custom Stellaris™ RNA FISH Probes was designed against the 5' open reading frame of CHIKV (strain LR2006-OPY1, GenBabk: DQ443544.2) by utilizing the Stellaris RNA FISH Probe Designer (LGC, Biosearch Technologies, Petaluma, CA) available online at www.biosearchtech.com/stellarisdesigner. Each probe was labeled with Quasar™ 570 dye (LGC, Biosearch Technologies, Petaluma, CA) and hybridized to CHIK21-infected human fibroblasts, according to the manufacturer's instructions available online at www.biosearchtech.com/stellarisprotocols. Briefly, following viral protein immunostaining (see section 'Immunofluorescence'), cells were washed three times with PBS and fixed with 2% (v/v) of PFA diluted in PBS for 10 min at room temperature. Cells were washed twice in PBS and incubated with Stellaris Wash Buffer A at room temperature for 10 min. Cells were incubated with RNA probes diluted at 0.125 nM final concentration in hybridization buffer supplemented with 0.5 mM vanidyl ribonucleoside complex, for 16 h in humidified chamber at 37 °C. Cells were first washed in Stellaris Wash buffer A for 30 min at 37 °C, and then with Stellaris Wash buffer B for 10 min. Slides were mounted with ProLong Gold antifade reagent containing DAPI for nuclear staining (Thermo Fisher Scientific). Of note, all buffers and reagents used were RNase-free. Fluorescence microscopy images were acquired using a LSM 800 confocal microscope (Zeiss).

Immunoblot

U2OS (3×10^6 cells) were grown on 6-well plates for 24 h. Cells were transfected with 2.5 µg of DNA expression plasmid using jetOPTIMUS® DNA Transfection Reagent (PolyPlus) according to the manufacturer's instructions. At 48 h after transfection, cells were washed with PBS, collected with cell scrapper and pelleted by centrifugation (400 g for 5 min). Cell pellets were lysed in Pierce™ IP Lysis Buffer (Thermo Fisher Scientific) containing Halt™ Protease and Phosphatase Inhibitor Cocktail (Thermo Fischer Scientific) for 30 min at 4 °C. Equal amount of protein, determined by DC™Protein Assay (BioRad), were prepared in LDS Sample Buffer 4X (Pierce™) containing 25 mM dithiothreitol (DTT) and heated at 95 °C for 5 min. Samples were separated on Bolt™ 4–12% Bis-Tris gels in Bolt® MOPS SDS Running Buffer (Thermo Scientific), and proteins were transferred onto a PVDF membrane (BioRad) using the Power Blotter system (Thermo Fischer Scientific). Membranes were blocked with PBS containing 0.1% Tween-20 and 5% non-fat dry milk and incubated overnight at 4 °C with primary antibody. Staining was revealed with corresponding horseradish peroxidase (HRP)-coupled secondary antibodies and developed using SuperSignal™ West Dura Extended Duration Substrate (Thermo Fisher Scientific) following manufacturer's instructions. The signals were acquired through Fusion Fx camera (VILBERT Lourmat).

Transmission electron microscopy

Cells were fixed for 24 h in 1% glutaraldehyde, 4% paraformaldehyde, (Sigma, St-Louis, MO) in 0.1 M phosphate buffer (pH 7.2). Samples were then washed in phosphate-buffered saline (PBS) and post-fixed for 1 h by incubation with 2% osmium tetroxide (Agar Scientific, Stansted, UK). Cells were then fully dehydrated in a graded series of ethanol solutions and propylene oxide. Impregnation step was performed with a mixture of (1:1) propylene oxide/Epon resin (Sigma) and then left overnight in pure resin. Samples were then embedded in Epon resin (Sigma), which was allowed to polymerize for 48 h at 60 °C. Ultra-thin sections (90 nm) of these blocks were obtained with a Leica EM UC7 ultramicrotome (Wetzlar, Germany). Sections were stained with 2% uranyl acetate (Agar Scientific), 5% lead citrate (Sigma) and observations were made with a transmission electron microscope (JEOL 1011, Tokyo, Japan).

Immunogold labeling of cryosections

Cells were fixed for 2 h with 4% paraformaldehyde in phosphate buffer (pH 7.6), washed with PBS (pH 7.6) for 2 × 5 min and centrifuged at 300 g for 10 min. After removing the supernatant, cell pellets were included in gelatin 12% and infused with sucrose 2.3 M overnight at 4 °C. 80 nm ultra-thin cryosections were made a −120 °C on a LEICA FC7 cryo-ultramicrotome. Ultra-thin sections were retrieved with Methylcellulose 2%/Sucrose 2.3 M mixture (1:1) and collected onto formvar/carbon coated nickel grids. After removal of gelatine at 37 °C, sections were incubated on drops of either 1:100 anti-nsP3 rabbit serum, anti-Capsid rabbit serum, anti-FHL1 monoclonal or anti-G3BP1 monoclonal antibody diluted in PBS. After six washes of 5 min each, grids were incubated on drops of PBS containing 1:30 gold-conjugated goat anti-rabbit or anti-mouse Ab (6 nm) (Aurion, Wageningen, Netherlands). Grids were finally washed with six drops of PBS (5 min each), post-fixed in 1% glutaraldehyde and rinsed with three drops of distilled water. Contrasting step was performed by incubating grids on drops of uranyl acetate 2% / methylcellulose 2% mixture (1:10). The sections were imaged in a transmission electron microscope at 100 kV (JEOL 1011).

Image processing and analysis

All confocal microscopy images were processed and analyzed with ImageJ (version: 2.9.0/1.53t)[37]. For aggregate quantification, cell boundaries were traced to delimitate each signal-positive cell. Aggregates' channel was extracted and automatic signal thresholding was applied to locate objects of interest. Images were binarized and Image J "*Analyze particles*" macro was used to quantify aggregates based on size (0.05–5 µm) and circularity (0.01-1) discrimination. For colocalization analysis, images were processed and Pearson's coefficient was calculated using BIOP JACoP plugin as described in https://imagej.net/plugins/jacop.

Statistical analysis

Graphical representation and statistical analyses were performed using Prism 9 software (GraphPad software). Unless otherwise stated, results are shown as mean ± s.e.m. from at least two independent experiments in duplicates. Differences were tested for statistical

significance one-way or two-way ANOVA with multiple comparison post hoc test.

Inclusions and ethics statements

The authors were committed to promoting inclusivity and diversity in all aspects of the research process. This includes fostering an environment of mutual respect and understanding among researchers of different genders, ethnicities, cultures, and backgrounds.

All research procedures were conducted in strict adherence to ethical guidelines and standards as set forth by INSERM, CNRS, and the respective universities involved. The authors are committed to upholding the principles of integrity, transparency, and accountability in the conduct of our research. Any potential conflicts of interest have been disclosed, and efforts were made to ensure that the research was conducted without bias, with an emphasis on scientific rigor and ethical responsibility.

Reporting summary

Further information on research design is available in the Nature Portfolio Reporting Summary linked to this article.

Data availability

The electron density maps and models generated in this study have been deposited in the Electron Microscopy and Protein Data Banks, respectively, as follows: The helical reconstruction map at 2.53 Å and model coordinates (EMD: 17729, PDB: 8PK7). The focus refinement map at 2,35 Å resolution and the refined model coordinates: (EMD: 17678, PDB: 8PHZ). For the map at showing the densities corresponding to the macrodomain with a resolution of 2.98 Å and the 3D focused classification map at 6.84 Å (EMD: 17730). The source data generated in this study for western blot, viral titrations, microscopy statistical analysis and luminescence read outs are provided in the Source Data file. The nsP3 protein sequences used in this study are available in the Uniprot database under accession codes Q8JUX6 for CHIK, P13886 for O'nyong-nyong virus (ONNV), P13887 for Ross river virus (RRV), Q8QZ73 for Mayaro virus (MAYV), Q4QXJ8 for Eastern equine encephalitis virus (EEEV), P36327 for Venezuelan equine encephalitis virus (VEEV), P87515 for Barmah forest virus (BFV), P03317 for Sindbis virus (SINDO), Q86924 for Aura virus (AURAV) and Q8JJX1 for Sleeping disease virus (SDV). Source data are provided with this paper.

References

1. Baxter, V. K. & Heise, M. T. Immunopathogenesis of alphaviruses. *Adv. Virus Res.* **107**, 315–382 (2020).
2. Kril, V., Aïqui-Reboul-Paviet, O., Briant, L. & Amara, A. New insights into chikungunya virus infection and pathogenesis. *Annu Rev. Virol.* **8**, 327–347 (2021).
3. Ahola, T., McInerney, G. & Merits, A. Alphavirus RNA replication in vertebrate cells. *Adv. Virus Res.* **111**, 111–156 (2021).
4. Frolov, I. & Frolova, E. I. Molecular virology of chikungunya virus. *Curr. Top. Microbiol. Immunol*. https://doi.org/10.1007/82_2018_146 (2019).
5. Vasiljeva, L. et al. Regulation of the sequential processing of Semliki forest virus replicase polyprotein. *J. Biol. Chem.* **278**, 41636–41645 (2003).
6. Shirako, Y. & Strauss, J. H. Regulation of Sindbis virus RNA replication: uncleaved P123 and nsP4 function in minus-strand RNA synthesis, whereas cleaved products from P123 are required for efficient plus-strand RNA synthesis. *J. Virol.* **68**, 1874–1885 (1994).
7. Gorchakov, R. et al. A new role for ns polyprotein cleavage in sindbis virus replication. *J. Virol.* **82**, 6218–6231 (2008).
8. Laurent, T. et al. Architecture of the Chikungunya virus replication organelle. *Elife* **11**, e83042 (2022).
9. Tan, Y. B. et al. Molecular architecture of the Chikungunya virus replication complex. *Sci. Adv.* **8**, eadd2536 (2022).
10. Jones, R., Bragagnolo, G., Arranz, R. & Reguera, J. Capping pores of alphavirus nsP1 gate membranous viral replication factories. *Nature* **589**, 615–619 (2021).
11. Shin, G. et al. Structural and functional insights into alphavirus polyprotein processing and pathogenesis. *Proc. Natl Acad. Sci. USA* **109**, 16534–16539 (2012).
12. Abraham, R. et al. ADP-ribosyl-binding and hydrolase activities of the alphavirus nsP3 macrodomain are critical for initiation of virus replication. *Proc. Natl Acad. Sci. USA* **115**, E10457–E10466 (2018).
13. Gao, Y., Goonawardane, N., Ward, J., Tuplin, A. & Harris, M. Multiple roles of the non-structural protein 3 (nsP3) alphavirus unique domain (AUD) during Chikungunya virus genome replication and transcription. *PLoS Pathog.* **15**, e1007239 (2019).
14. Meertens, L. et al. FHL1 is a major host factor for chikungunya virus infection. *Nature* **574**, 259–263 (2019).
15. Meshram, C. D. et al. Multiple host factors interact with hypervariable domain of Chikungunya virus nsP3 and determine viral replication in cell-sapecific mode. *J. Virol*. https://doi.org/10.1128/JVI.00838-18 (2018).
16. Fros, J. J. et al. Chikungunya virus nsP3 blocks stress granule assembly by recruitment of G3BP into cytoplasmic foci. *J. Virol.* **86**, 10873–10879 (2012).
17. Jumper, J. et al. Highly accurate protein structure prediction with AlphaFold. *Nature* **596**, 583–589 (2021).
18. Remenyi, R. et al. Persistent replication of a Chikungunya virus replicon in human cells is associated with presence of stable cytoplasmic granules containing nonstructural protein 3. *J. Virol.* **92**, e00477–18 (2018).
19. Bartholomeeusen, K. et al. A Chikungunya virus trans-replicase system reveals the importance of delayed nonstructural polyprotein processing for efficient replication complex formation in mosquito cells. *J. Virol.* **92**, e00152–18 (2018).
20. Ng, W. H. et al. FHL1 promotes Chikungunya and O'nyong-nyong virus infection and pathogenesis with implications for alphavirus vaccine design. *Nat. Commun.* **14**, 6605 (2023).
21. Kim, D. Y. et al. New world and old world alphaviruses have evolved to exploit different components of stress granules, FXR and G3BP proteins, for assembly of viral replication complexes. *PLoS Pathog.* **12**, e1005810 (2016).
22. Foy, N. J. et al. Hypervariable domains of nsP3 proteins of new world and old world alphaviruses mediate formation of distinct, virus-specific protein complexes. *J. Virol.* **87**, 1997–2010 (2013).
23. Zheng, Y. & Kielian, M. Imaging of the alphavirus capsid protein during virus replication. *J. Virol.* **87**, 9579–9589 (2013).
24. Lello, L. S. et al. nsP4 is a major determinant of alphavirus replicase activity and template selectivity. *J. Virol.* **95**, e0035521 (2021).
25. Snyder, J. E. et al. Rescue of infectious particles from preassembled alphavirus nucleocapsid cores. *J. Virol.* **85**, 5773–5781 (2011).
26. Fontana, J., López-Montero, N., Elliott, R. M., Fernández, J. J. & Risco, C. The unique architecture of bunyamwera virus factories around the golgi complex. *Cell Microbiol* **10**, 2012–2028 (2008).
27. Barski, M. et al. Rift Valley fever phlebovirus NSs protein core domain structure suggests molecular basis for nuclear filaments. *eLife* **6**, e29236 (2017).
28. Gutsche, I. et al. Structural virology. Near-atomic cryo-EM structure of the helical measles virus nucleocapsid. *Science* **348**, 704–707 (2015).
29. Le Sage, V. et al. Ebola virus VP35 blocks stress granule assembly. *Virology* **502**, 73–83 (2017).
30. Kandiah, E. et al. CM01: a facility for cryo-electron microscopy at the European synchrotron. *Acta Crystallogr D. Struct. Biol.* **75**, 528–535 (2019).
31. de la Rosa-Trevín, J. M. et al. Scipion: A software framework toward integration, reproducibility and validation in 3D electron microscopy. *J. Struct. Biol.* **195**, 93–99 (2016).

32. Punjani, A., Rubinstein, J. L., Fleet, D. J. & Brubaker, M. A. cryoSPARC: algorithms for rapid unsupervised cryo-EM structure determination. *Nat. Methods* **14**, 290–296 (2017).
33. Mirdita, M. et al. ColabFold: making protein folding accessible to all. *Nat. Methods* **19**, 679–682 (2022).
34. Schuffenecker, I. et al. Genome microevolution of chikungunya viruses causing the Indian Ocean outbreak. *PLoS Med.* **3**, e263 (2006).
35. Levitt, N. H. et al. Development of an attenuated strain of chikungunya virus for use in vaccine production. *Vaccine* **4**, 157–162 (1986).
36. Kümmerer, B. M., Grywna, K., Gläsker, S., Wieseler, J. & Drosten, C. Construction of an infectious Chikungunya virus cDNA clone and stable insertion of mCherry reporter genes at two different sites. *J. Gen. Virol.* **93**, 1991–1995 (2012).
37. Bolte, S. & Cordelières, F. P. A guided tour into subcellular colocalization analysis in light microscopy. *J. Microsc.* **224**, 213–232 (2006).

Acknowledgements

A.A.'s lab received fundings from the French Government's Investissement d'Avenir program, Laboratoire d'Excellence "Integrative Biology of Emerging Infectious Diseases" (grant n°ANR-10-LABEX-62- IBEID), the Fondation pour la Recherche Medicale (FRM équipe - EQU202003010193), the Agence Nationale de la Recherche (project CHIKHOST ANR-20-CE15-0029, project COALITION ANR-20-CE92-0054 and project CHIKMac ANR-22-CE11 0023), INSERM transfert and l'Association Française pour la Myopathie (AFM, grant *23270)*. J.R's team was supported by grants of the Agence Nationale de la Recherche (project CHIKmac ANR-22-CE11-0023-01 and project CoMemRep ANR-20-COV3-0004) and the Fondation Bettencourt Shueller (AGDI-531281), ATIP-Avenir grant (CNRS/INSERM). B.M.K received funding from the Deutsche Forschungsgemeinschaft (DFG, German Research Foundation, Project ID 369799452-TRR237). We thank the European Synchrotron Radiation Facility for provision of beam time on CM01. We used the Integrated structural biology facility (PBSIM) at the AFMB supported by French Infrastructure for Integrated Structural Biology (FRISBI) (ANR-10-INBS-0005). J.R. work was granted access to the HPC resources of IDRIS under the dynamic allocation AD010315372. V.K is supported by a fellowship from University de Paris Cité. A.K. is supported by a CENTURI PhD fellowship financed by "Investissements d'Avenir" program (ANR-16-CONV-0001) and from Excellence Initiative of Aix-Marseille University - A*MIDEX. The authors are grateful to Pr Andres Merits (University of Tartu, Estonia) for providing us anti-nsP1-4 antibodies and CHIKV P1234 plasmids, to Pr Mark Harris (Univeristy of Leeds, UK) for the CHIKV replicon and to Pr Valérie Choumet (Pasteur Institute, France) for providing the anti-CHIKV E2 Mab 3E4. The authors thank Pr Olivier Schwartz and Pr. Alessia Zamborlini for critical readings of the manuscript and helpful discussions.

Author contributions

A.A and J.R designed and coordinated the research. V.K generated and characterized the FLAG-tagged nsP3, AUD plasmids and lentiviruses. V.K performed viral infection studies, RNA-FISH experiments, confocal microscopy, image processing and analysis and western blot studies. M.H. carried out the data collection, processing and volume reconstructions with the input of A.D. for helical reconstruction. C.A generated the in vitro transcribed viral RNA and performed the infection and functional studies (mutant characterization and SINV experiments). L.C and Y.B produced and titrated the CHIKV and alphavirus stocks used in this work and performed infection studies. L.M and J.B.G performed the first experiments that allowed the identification of nsP3 tubes in CHIKV-infected cells. L.M participated in the functional studies and manuscript preparation. J.B.G and P.R. performed the EM experiments. A.T and B.M.K. generated the CHIKV and SINV molecular clones. R.J and C.Z isolated, identified and biochemically characterized the nsP3 tubes. A.K. produced the nsP3 mutants in Hi-5cells and performed the in vitro assembly studies. D.P. vitrified the samples for cryo-EM. J.R did the model building, analysis and refinement. A.A. and J.R. wrote the initial manuscript draft and the other authors contributed to its editing in its final form.

Competing interests

The authors declare no competing interests.

Additional information

Supplementary information The online version contains supplementary material available at https://doi.org/10.1038/s41467-024-51952-z.

Correspondence and requests for materials should be addressed to Ali Amara or Juan Reguera.

Peer review information *Nature Communications* thanks the anonymous reviewers for their contribution to the peer review of this work. A peer review file is available.